

# **BACHELOR PAPER**

Term paper submitted in partial fulfillment of the requirements  
for the degree of Bachelor of Science in Engineering at the  
University of Applied Sciences Technikum Wien - Degree  
Program TW

## **Semi-automatic Liver Segmentation in Low- contrast CT Images: Comparison between a Gradient Vector Flow Snake and a Morpho- logical Geodesic Active Contour**

By: Oskar Petto

Student Number: 1310227042

Supervisor: DI Dr. techn. Matthias Blaickner

Vienna, May 11, 2016

# Declaration

"As author and creator of this work to hand, I confirm with my signature knowledge of the relevant copyright regulations governed by higher education acts (for example see §§21, 46 and 57 UrhG (Austrian copyright law) as amended as well as §11 of the Statute on Studies Act Provisions / Examination Regulations of the UAS Technikum Wien).

In particular I declare that I have made use of third-party content correctly, regardless what form it may have, and I am aware of any consequences I may face on the part of the degree program director if there should be evidence of missing autonomy and independence or evidence of any intent to fraudulently achieve a pass mark for this work (see §11 para. 1 Statute on Studies Act Provisions / Examination Regulations of the UAS Technikum Wien).

I further declare that up to this date I have not published the work to hand nor have I presented it to another examination board in the same or similar form. I affirm that the version submitted matches the version in the upload tool.“

Vienna, May 11, 2016

Place, Date

A handwritten blue ink signature consisting of two stylized, cursive loops.

Signature

## Kurzfassung

Medizinische Bildsegmentierung wird verwendet für anatomische Studien, zur Quantifizierung von Volumen, Lokalisation von Pathologien und für die Behandlungsplanung in der Strahlentherapie. Die vorliegende Arbeit untersucht die Abweichungen von parametrischen und geometrischen, verformbaren Modellen bei der Lebersegmentierung in Computer Tomographie (CT) Aufnahmen mit niedrigem Kontrast aufgrund ähnlicher Grauwerte in angrenzenden Organen. Ein Gradient Vector Flow (GVF) Snake Algorithmus und ein morphologischer Geodesic Active Contour (GAC) Algorithmus wurden implementiert, um die Leber als slice-by-slice Technik von einzelnen CT Schichtbildern zu segmentieren. Beide Algorithmen wurden an CT Aufnahmen mit geringem Kontrast von 21 Patienten getestet und mit einer manuellen Segmentierung von Huber [1] anhand von relativer Volumsdifferenz (RVD), Volumen-Überlapungsfehler (VOE) und Dice Ähnlichkeitskoeffizient (DS) verglichen. Die Ergebnisse sind als Mittelwert und Standardabweichung von allen 21 Patienten angegeben. Der GVF Snake Algorithmus erreichte eine RVD von  $-11.4 \pm 9.3\%$ , einen VOE of  $25.7 \pm 7.2\%$  und einen DS von  $0.85 \pm 0.05$ . Der morphologische GAC Algorithmus brachte einen RVD von  $-3.9 \pm 6.1\%$ , einen VOE von  $17.3 \pm 2.8\%$  und einen DS von  $0.91 \pm 0.02$  zustande. Für eine Lebersegmentierung benötigte der GVF Snake Algorithmus 2 bis 7 Minuten und der morphologische GAC Algorithmus 30 bis 70 Sekunden. Demnach ist der morphologische GAC Algorithmus besser geeignet für die Lebersegmentierung in CT Aufnahmen mit geringem Kontrast für Weichteilgewebe. Jedoch sind weitere Verbesserungen notwendig um die benötigte Genauigkeit und Robustheit für die Anwendung in der klinischen Praxis zu erreichen.

**Schlagworte:** Lebersegmentierung, CT, geringer Kontrast, GVF snake, Morphologische GAC

# Abstract

Medical image segmentation is essential for anatomical studies, volume quantification, localization of pathology and treatment planning for radiotherapy. This thesis aims to investigate the deviations of parametric and geometric deformable models regarding liver segmentation in low-contrast Computed Tomography (CT) images, which is particularly challenging due to similar gray levels in adjacent organs. For this reason a gradient vector flow (GVF) snake algorithm and a morphological geodesic active contour (GAC) algorithm were implemented to segment the liver as a slice-by-slice technique from individual CT slices. Both algorithms were tested on low-contrast CT datasets from 21 patients and evaluated on the basis of a manual segmentation performed by Huber [1] with regard to relative volume difference (RVD), volume overlap error (VOE) and dice similarity coefficient (DS). The GVF snake algorithm achieved a RVD of  $-11.4 \pm 9.3\%$ , a VOE of  $25.7 \pm 7.2\%$  and a DS  $0.85 \pm 0.05$ . The morphological GAC algorithm scored a RVD of  $-3.9 \pm 6.1\%$ , a VOE of  $17.3 \pm 2.8\%$  and a DS of  $0.91 \pm 0.02$ . The computation time per liver segmentation was between 30 and 70 seconds for the morphological GAC algorithm and between 2 and 7 minutes for the GVF snake algorithm. Therefore the morphological GAC algorithm is better suited for liver segmentation in low-contrast CT images. However further improvements are needed to achieve the accuracy and robustness for the clinical application.

**Keywords:** Liver segmentation, Low-contrast CT, GVF snake, Morphological GAC

# Acknowledgements

I would like to thank DI Dr. techn. Matthias Blaickner for his advice and extensive support during the writing of this thesis and Martin Dulovits for some tips before the implementation of the GVF snake algorithm. Furthermore I thank Iris Petto for her help regarding editorial choices.

My thanks also goes to the European Neuroendocrine Tumour Society (ENETS) Center of Excellence at the Zentralklinik Bad Berka and to the Department of Radiation Oncology in the Division of Medical Radiation Physics from the Christian Doppler Laboratory for Medical Radiation Research for Radiation Oncology at the Medical University of Vienna for providing the low-contrast CT datasets.

# Contents

<b>1</b>	<b>Introduction</b>	<b>1</b>
1.1	Medical Image Segmentation . . . . .	1
1.2	Deformable Models . . . . .	2
1.2.1	Parametric models . . . . .	2
1.2.2	Geometric models . . . . .	5
1.3	Morphological Operations . . . . .	6
<b>2</b>	<b>Methods</b>	<b>9</b>
2.1	Implementation details . . . . .	9
2.1.1	GVF snake algorithm . . . . .	10
2.1.2	Morphological GAC algorithm . . . . .	13
2.2	Evaluation . . . . .	15
<b>3</b>	<b>Results</b>	<b>17</b>
<b>4</b>	<b>Discussion</b>	<b>19</b>
4.1	Conclusion . . . . .	21
<b>Bibliography</b>		<b>22</b>
<b>List of Figures</b>		<b>26</b>
<b>List of Tables</b>		<b>27</b>
<b>List of Abbreviations</b>		<b>28</b>

# 1 Introduction

This thesis provides a short introduction to liver segmentation in low-contrast Computed Tomography (CT) images and the basics of deformable models, a commonly used class of image segmentation techniques. The main focus lies on the methodical differences between parametric and geometric deformable models and their deviations regarding liver segmentation. The parametric deformable model was implemented in form of a gradient vector flow (GVF) snake and the geometric deformable model was chosen to be a morphological geodesic active contour (GAC) based on the algorithm from Márquez et al. [2]. Both algorithms were designed to segment the liver as a slice-by-slice technique from individual CT slices, i.e. the algorithm tries to find the organ's boundary in a given transverse plane and then segments one plane after another. To evaluate the segmentation differences they were tested on 21 low-contrast CT datasets and the results were compared to manual liver segmentations performed by Huber [1].

## 1.1 Medical Image Segmentation

Segmentation is the process in which an image is divided into regions with similar properties. Image segmentation generally plays an important role in medical imaging as it can be used to separate different tissue regions. Medical image segmentation is used in a variety of applications such as anatomical studies, volume quantification, localization of pathology and treatment planning for radiotherapy [3].

Compared to manual delineation, computational image segmentation aims for faster, more accurate and more reproducible results, especially when processing large datasets. However there occur certain image-related problems in CT images which cause computerized image segmentation to be a challenging task. These problems are noise, artefacts and partial volume effect of the images. Applications of medical image segmentation are very diverse and there is no universal algorithm. Instead several different segmentation algorithms are available, each of them designed for a specific task [3].

Some segmentation tasks are more difficult than others. Liver segmentation in CT images is a particular challenge due to similar gray levels in adjacent organs, such as pancreas or stomach. Furthermore ligaments inside the liver (e.g. falciform ligament) as well as blood vessels cause gray level variations and might be misconstrued as organ boundaries [4, 5].

Available methods for medical image segmentation include thresholding, region growing, active contours, level sets, atlas-based segmentation, statistical shape models and Markov random fields. This thesis solely focuses on active contours and the level set method, which fall under the category of deformable models. [6, 7]

## 1.2 Deformable Models

Deformable models are curves or surfaces which are defined within the image domain and subsequently deformed under the influence of internal and external forces. Internal forces ensure a smooth shape during deformation and are derived from the model itself. External forces are calculated from the image data and move the model towards the desired image features, such as organ boundaries. Deformable models have been widely used in medical image segmentation due to their robustness with regard to boundary gaps and image noise. One can distinguish between parametric and geometric models [8, 9].

### 1.2.1 Parametric models

Parametric models use an explicit representation of a curve or surface, i.e. the model is represented by a set of control points and thus can be directly deformed. In a two-dimensional image domain parametric models are usually called snakes or active contours, whereas one refers to deformable surfaces in a three-dimensional domain [9].

Kass et al. [10] introduced active contours as parametrically defined curves as a set of vectors of the form  $\mathbf{x}(s) = (x(s), y(s))$ , where  $x(s)$  and  $y(s)$  are the coordinates of point  $s$  in the two-dimensional image domain. Active contours are deformed by minimizing the energy functional

$$E = \int_0^1 E_{int}(\mathbf{x}(s)) + E_{ext}(\mathbf{x}(s))ds. \quad (1)$$

This functional is dependent on the internal and external energy functions  $E_{int}$  and  $E_{ext}$  of the curve  $\mathbf{x}(s)$  and the first term can be written as

$$E_{int}(\mathbf{x}(s)) = \frac{1}{2}(\alpha|\mathbf{x}_s(s)|^2 + \beta|\mathbf{x}_{ss}(s)|^2), \quad (2)$$

where  $\alpha$  controls the first-order term that makes the snake act like a membrane and  $\beta$  controls the second-order term which makes it act like a thin plate. In other words a high  $\alpha$  discourages stretching and a high  $\beta$  discourages bending [10]. The energy minimized snake has to satisfy the Euler equation

$$\alpha\mathbf{x}_{ss}(s) - \beta\mathbf{x}_{ssss}(s) - \nabla E_{ext} = 0. \quad (3)$$

This can be seen as a force balance equation that is solved by treating the snake  $\mathbf{x}(s)$  as a function of time  $t$ . The partial derivative of  $\mathbf{x}(s, t)$  with respect to  $t$  can then be written as

$$\mathbf{x}_t(s, t) = \alpha \mathbf{x}_{ss}(s, t) - \beta \mathbf{x}_{ssss}(s, t) - \nabla E_{ext}. \quad (4)$$

The numerical solution to (4) is used to iteratively calculate the contour deformation for a given step-size. There are different external energy functions  $E_{ext}$  available for computing external forces from image data. External forces can be static, such as the potential force for traditional snakes, or dynamic, such as a balloon force that moves the contour in its normal direction. The potential force can be obtained by calculating the negative gradient of the grayscale image [11].

### Gradient Vector Flow

Traditional potential forces have a small capture range, which requires the initial contour to be placed close to the true object boundary. Additionally the conversion to concave boundaries of snakes driven by potential forces is generally poor. Xu and Prince [12] introduced the gradient vector flow (GVF) field as an alternative, static external force for snakes. A GVF field is a dense vector field of the form  $\mathbf{v}(x, y) = (u(x, y), v(x, y))$ , with  $x$  and  $y$  representing the two-dimensional image domain. It is obtained by minimization of the energy functional

$$E = \iint \mu(u_x^2 + u_y^2 + v_x^2 + v_y^2) + |\nabla f|^2 |\mathbf{v} - \nabla f|^2 dx dy, \quad (5)$$

where  $f$  is an edge map of the image and  $\nabla f$  is a vector field directing toward edges in the image. The energy functional can be controlled by the parameter  $\mu$ , which should be set in direct relation to the amount of image noise. The GVF field satisfies the following Euler equations

$$\mu \nabla^2 u - (u - f_x)(f_x^2 + f_y^2) = 0, \quad (6)$$

$$\mu \nabla^2 v - (v - f_y)(f_x^2 + f_y^2) = 0. \quad (7)$$

The bigger capture range results from the first term moving the contour in regions where no edges are present and the gradient of  $f(x, y)$  is zero. The solution to equations (6) and (7) can be found by treating  $u$  and  $v$  as functions of time  $t$  [12]. The associated equations for  $u(x, y, t)$  and  $v(x, y, t)$  can be written as

$$u_t(x, y, t) = \mu \nabla^2 u(x, y, t) - (u(x, y, t) - f_x(x, y))(f_x(x, y)^2 + f_y(x, y)^2), \quad (8)$$

$$v_t(x, y, t) = \mu \nabla^2 v(x, y, t) - (v(x, y, t) - f_y(x, y))(f_x(x, y)^2 + f_y(x, y)^2). \quad (9)$$

By defining  $b(x, y) = f_x^2(x, y) + f_y^2(x, y)$ ,  $c^1(x, y) = b(x, y)f_x(x, y)$  and  $c^2(x, y) = b(x, y)f_y(x, y)$  equations (8) and (9) become [13]

$$u_t(x, y, t) = \mu \nabla^2 u(x, y, t) - b(x, y)u(x, y, t) + c^1(x, y), \quad (10)$$

$$v_t(x, y, t) = \mu \nabla^2 v(x, y, t) - b(x, y)v(x, y, t) + c^2(x, y). \quad (11)$$

Using the subscript  $i, j$  instead of  $(x, y)$  and the superscript  $n$  instead of the time  $t$ ,  $\nabla^2 u$  and  $\nabla^2 v$  is computed according to [13]

$$\nabla^2 u = u_{i+1,j}^n + u_{i-1,j}^n + u_{i,j+1}^n + u_{i,j-1}^n - 4u_{i,j}^n, \quad (12)$$

$$\nabla^2 v = v_{i+1,j}^n + v_{i-1,j}^n + v_{i,j+1}^n + v_{i,j-1}^n - 4v_{i,j}^n. \quad (13)$$

With the use of equations (12) and (13), the iterative numerical method for computing the GVF field from the edge map can be written as [13]

$$u_{i,j}^{n+1} = (1 - b_{i,j} - 4\mu)u_{i,j}^n + \mu(u_{i+1,j}^n + u_{i-1,j}^n + u_{i,j+1}^n + u_{i,j-1}^n) + c_{i,j}^1, \quad (14)$$

$$v_{i,j}^{n+1} = (1 - b_{i,j} - 4\mu)v_{i,j}^n + \mu(v_{i+1,j}^n + v_{i-1,j}^n + v_{i,j+1}^n + v_{i,j-1}^n) + c_{i,j}^2, \quad (15)$$

Solving equations (14) and (15) iteratively for a certain time-step ultimately leads to the solution of the Euler equations (6) and (7). The resulting GVF field  $v$  can be used as an external force for snakes and equation (4) becomes

$$\mathbf{x}_t(s, t) = \alpha \mathbf{x}_{ss}(s, t) - \beta \mathbf{x}_{ssss}(s, t) + \mathbf{v}(s). \quad (16)$$

As the GVF field has to be calculated for the whole image domain, the computational time becomes exceedingly long for large images. To address this problem multigrid methods were introduced to efficiently solve the GVF equations (6) and (7) [14].

Parametric models can be used for many different segmentation problems, but two limitations make them difficult to use in certain applications, as described in [9]:

- They need to be reparametrized in situations where the initial model has a completely different shape and size than the desired object boundaries.
- Topology changes, such as splitting and merging require difficult methods for constructing new parametrizations.

### 1.2.2 Geometric models

Geometric models do not have these limitations, because they use an implicit representation of a curve or surface. This means instead of a fixed set of points the model is defined as a level set of a scalar function, which is called the level set function (LSF). This makes geometric models flexible in their topology and allows splitting and merging of the curve or surface [15].

The LSF is one dimension higher than the image domain and the level set is defined as a set where the LSF takes on the same value. The initial LSF is computed as a signed distance function in the image domain with the initial curve being the zero level set and with positive values inside the contour. The curve evolution is calculated by updating the LSF for a specific time-step at fixed image coordinates [9]. In order to move a curve  $C$  in its normal direction, the LSF  $u$  has to be deformed according to

$$u_t = F|\nabla u|, \quad (17)$$

where  $F$  is a speed function that can be computed from the image or the LSF [16]. Caselles et al. [17] introduced the geodesic active contour (GAC) model and the partial derivative of its LSF with respect to time  $t$  as

$$u_t = g(I)|\nabla u|\operatorname{div}\left(\frac{\nabla u}{|\nabla u|}\right) + g(I)|\nabla u|\nu + \nabla g(I)\nabla u, \quad (18)$$

where

$$\begin{aligned} g(I)|\nabla u|\operatorname{div}\left(\frac{\nabla u}{|\nabla u|}\right) &\text{ is the curvature term} \\ g(I)|\nabla u|\nu &\text{ is the balloon term} \\ \nabla g(I)\nabla u &\text{ is the image attraction term} \end{aligned}$$

The curvature term from equation (18) keeps the contour smooth, the balloon term moves the contour with constant speed and makes it converge faster and the image attraction term is able to pull it to object boundaries [17]. The function  $g(I)$  is computed as an external force from the image  $I$  and stops the contour at the object boundaries. Caselles et al. [18] defined  $g(I)$  as

$$g(I) = \frac{1}{1 + |\nabla \hat{I}|^p}, \quad (19)$$

where  $\hat{I}$  is the image smoothed with a filter, such as the Gaussian filter, and  $p$  is usually set to 1 or 2. Another common definition of  $g(I)$  is

$$g(I) = \exp(-|\nabla \hat{I}|^p). \quad (20)$$

The stopping function  $g(I)$  takes on values closer to zero near object boundaries and values closer to one in homogeneous regions. The image attraction term uses  $\nabla g(I)$  in order to point toward the center within the boundary region [17].

The main drawback of the GAC model compared to the classical snakes is that the numerical time step is limited due to stability of the explicit Euler schemes, which results in inefficient implementations. Narrow band techniques [19], additive operator splitting [20] and the fast marching method for re-initialization of the LSF [16] can speed up the associated computations [21]. Multigrid methods can also be used in conjunction with the GAC model [22].

### 1.3 Morphological Operations

In image processing morphological operations are used to manipulate the geometric structure within a binary or grayscale image. Morphological operators evaluate the fit of a structuring element with an image. Figure 1 shows a binary image with a structuring element placed at two different locations [23].

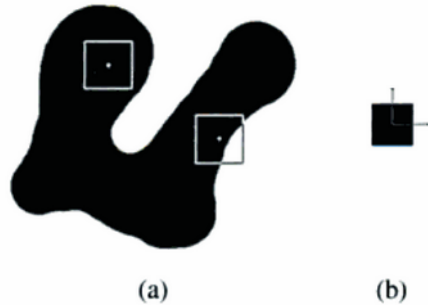


Figure 1: (a) Binary image with (b) structuring element placed at two locations, taken from [23]

Placing a structuring element at every position of a binary image, the overlap of the structuring element with the foreground of the binary image varies at different positions. One can derive structural information of an image by marking positions, where the structuring element fits the image. The result of a morphological operation is strongly influenced by the size and the shape of the structuring element [23].

The most basic morphological operations are binary erosion and binary dilation. A dilation of a binary image  $A$  by a structuring element  $B$  is denoted by  $A \oplus B$  and is defined by

$$A \oplus B = \bigcup_{b \in B} A_b = B \oplus A = \bigcup_{a \in A} B_a, \quad (21)$$

because dilation is commutative. The result of a binary dilation  $A \oplus B$  corresponds to an expansion of the image foreground, because it represents all positions, where  $A$  and  $B$  adjoin each other. Figure 2 shows a dilation of a binary image by a structuring element in the shape of a disk [23].

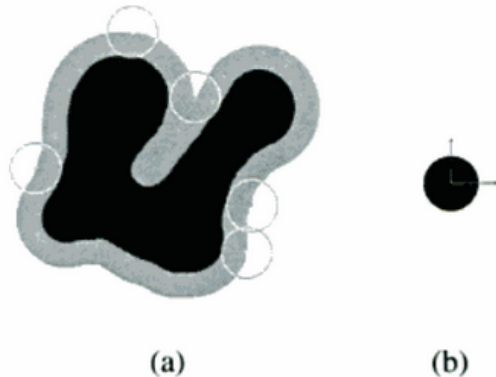


Figure 2: (a) Dilation of a binary image by (b) a disk, taken from [23]

An erosion of a binary image  $A$  by a structuring element  $B$  is denoted by  $A \ominus B$  and is defined by

$$A \ominus B = \bigcap_{b \in B} A_{-b}. \quad (22)$$

The result of a binary erosion  $A \ominus B$  can be described as all positions where  $B$  fits inside  $A$  and thus has the effect of shrinking the image foreground if the point of origin lies inside  $B$ . Figure 3 shows an erosion of a binary image by a structuring element element in the shape of a rectangle combined with a semi-disk [23].

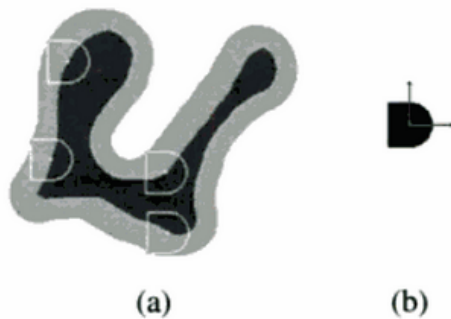


Figure 3: (a) Erosion of a binary image by (b) a rectangle combined with a semi-disk, taken from [23]

A binary LSF  $u$  contains the active contour at the 0.5 level set and its deformation according to equation (17) with  $F = 1$  is equivalent to a binary dilation  $D_h$  of  $u$  according to

$$|\nabla u| = \lim_{h \rightarrow 0^+} \frac{D_h u - u}{h}, \quad (23)$$

where  $h$  is the radius of the structuring element. A binary erosion  $E_h$  of  $u$  using a very small structuring element with the radius  $h$  is equal to

$$\lim_{h \rightarrow 0^+} \frac{E_h u - u}{h} = -|\nabla u|, \quad (24)$$

which solves equation (17) for  $F = -1$  [24]. Using these relations the morphological operators  $D_h$  and  $E_h$  can be used to approximate level set evolutions [2].

Márquez et al. [2] introduced a curvature morphological operator for approximating the curvature term from equation (18) for level set evolutions in any dimension. The discrete version of this operator for binary LSFs is denoted as  $SI_d \circ IS_d$ , where  $SI_d$  works on active pixels and  $IS_d$  only works on inactive pixels. The mathematical definition of  $SI_d \circ IS_d$  is outlined in the work of Márquez et al. [2]. For these operations four different 3x3 structuring elements are used, which can be seen in Figure 4.

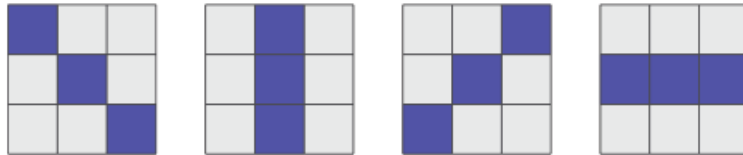


Figure 4: Four 3x3 structures for the discrete curvature morphological operator (dark blue = active), taken from [2]

The  $IS_d$  operator first performs four binary dilations with each of these structuring elements and then computes the element-wise minimum of the results. Analogously the  $SI_d$  operator is equivalent to the element-wise maximum of four binary erosions with the structuring elements from Figure 4. The  $SI_d \circ IS_d$  operator has the effect of switching pixels, where no straight lines of matching pixels are found, which results in a global smoothing of the binary LSF and thus removes edges in the contour [2].

Compared to regular numerical algorithms, the usage of morphological operations for the approximation of the level set evolution from equation (18) can reduce computational time. Additionally the morphological GAC algorithm is stable without any requirements for reinitialization and considerably easier to implement [2].

## 2 Methods

The majority of papers and book chapters referenced in this thesis were freely available online. Access to the publications from the IEEE Xplore® Digital Library was provided by the Austrian Institute of Technology (AIT). The following words and phrases were used for online searches of papers written in English: "Liver segmentation", "Medical image segmentation", "Liver CT", "Liver anatomy", "Deformable models", "Active Contours", "Snakes", "Gradient Vector Flow", "Multigrid methods", "Level sets", "Geometric deformable models", "Geodesic Active Contour", "Morphological operations", "Morphological snakes", "Comparison liver segmentation" and "Statistical shape model", "Statistical level set", "Radiotherapy image segmentation" and "Commercial segmentation system".

### 2.1 Implementation details

The GVF snake and the morphological GAC algorithms were designed for 2D liver segmentation in low-contrast CT images and were implemented in Python 2.7 with the use of the NumPy [25], SciPy [26] and OpenCV [27] libraries for calculations and the Matplotlib [28] library for visualization.

In the following description the term "slice" always refers to the transverse plane. The first step of both algorithms is to select all slices showing the liver, which is done by manually selecting the first and the last file. Next the user chooses the start file for the first segmentation which should be the slice located at the biggest extent of the liver. In order to speed up both algorithms a rectangular bounding box is manually placed with two mouse clicks to cut out the liver in the start slice. For each slice the same bounding box is used.

The finished segmentation of the start slice results in a final contour, which is diminished in size and taken as the initial contour for the adjacent slices. This process is repeated in one direction until the last slice is reached and afterwards the segmentation is continued from the start slice in the other z-direction. The segmentations of the GVF snake and the morphological GAC algorithms equal binary masks for every slice with 1 inside the final contour and 0 outside. Both algorithms were used to segment the liver in low-contrast CT datasets from 21 patients and afterwards the segmentations were evaluated as described in section 2.2.

### 2.1.1 GVF snake algorithm

After the CT image is cut to the selected bounding box image noise is reduced for each slice by applying an anisotropic diffusion filter [29], which regionally blurs images without removing image details such as edges. The number of iterations for the diffusion process was set proportional to the size of the bounding box and thus is inversely related to the pixel spacing. Pixel spacing co-determines voxel size, which influences the noise level of CT images [30]. The result of the filtering can be seen in Figure 5 for the bounding box of the start slice of patient 9.

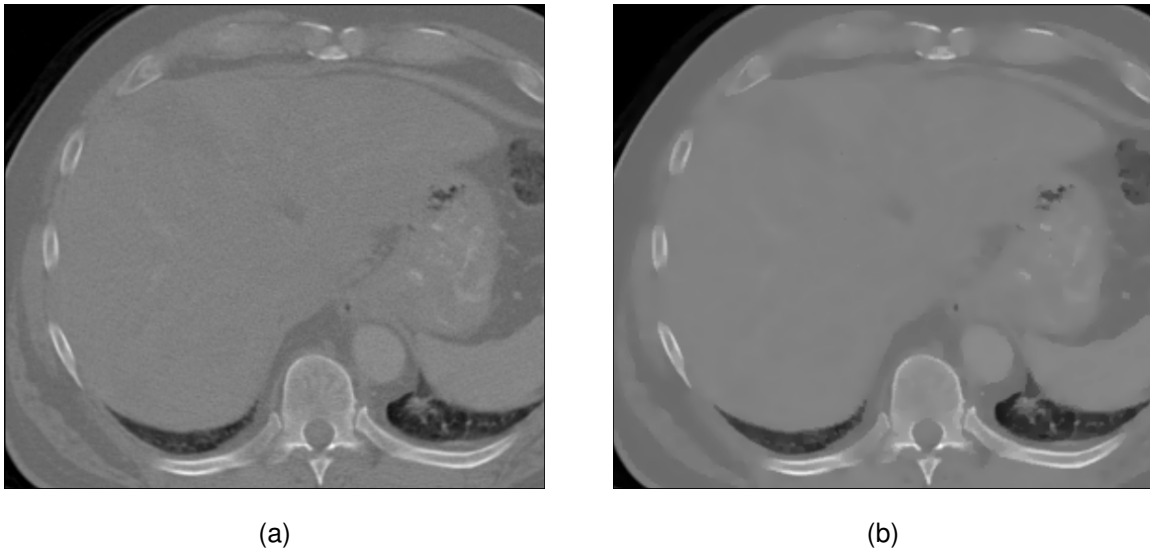


Figure 5: CT image (a) before and (b) after anisotropic diffusion filtering

A Canny edge detector [31] is then used to compute an edge map of the CT image with the high and low thresholds being proportional to the gray levels of soft tissue, i.e. to the brightness. As shown in Figure 6 the Canny algorithm also detects small edges inside the liver, which can prevent the GVF snake from reaching the liver boundary and therefore need to be removed. For this reason a structuring element with a square is placed at every possible position within the edge map and at positions with no intersections to edges, i.e. where the edge is completely inside the square, these edges are removed. This method is greatly influenced by the size of the square in the structuring element. Figure 6 shows the result for a 39x39 pixel square.

The modified edge map is used to calculate the GVF field according to equations (14) and (15), in 10 iterations with the parameter  $\mu$  being 0.2. The GVF field is then normalized with vector lengths in the range (0, 1) and the result can be seen in Figure 7. Next the user places the initial contour on the start slice by either multiple clicks inside the liver in the proximity of its boundaries or two clicks inside the liver for the centre and the radius of a circle. The number of placed points is only dependent on the size of the bounding box. While the first method uses linear interpolation for automatically placing equally spaced points between the points from the

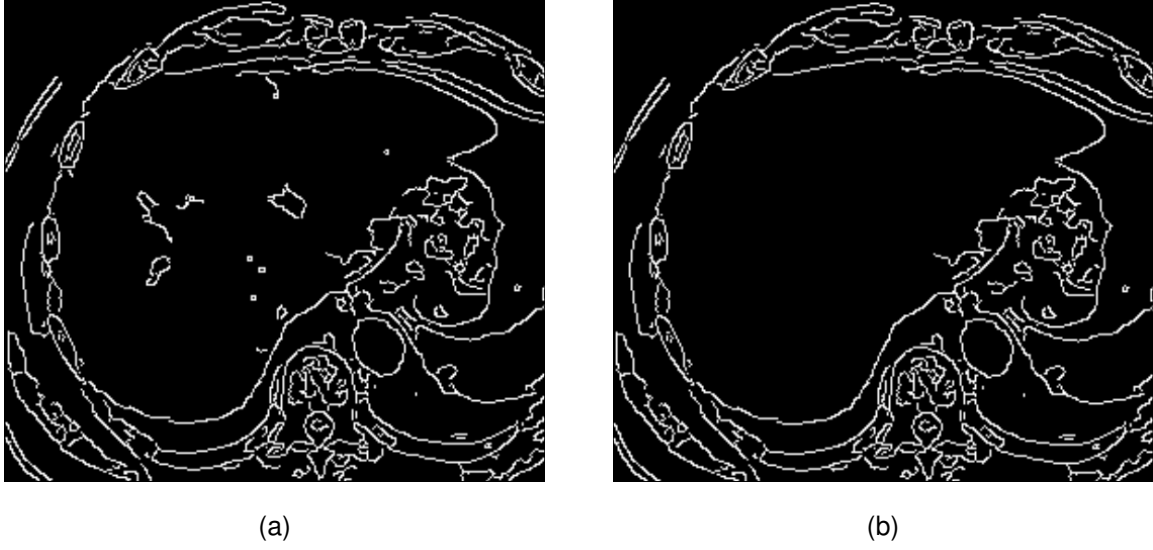


Figure 6: Edge map (a) before and (b) after the removal of small edges

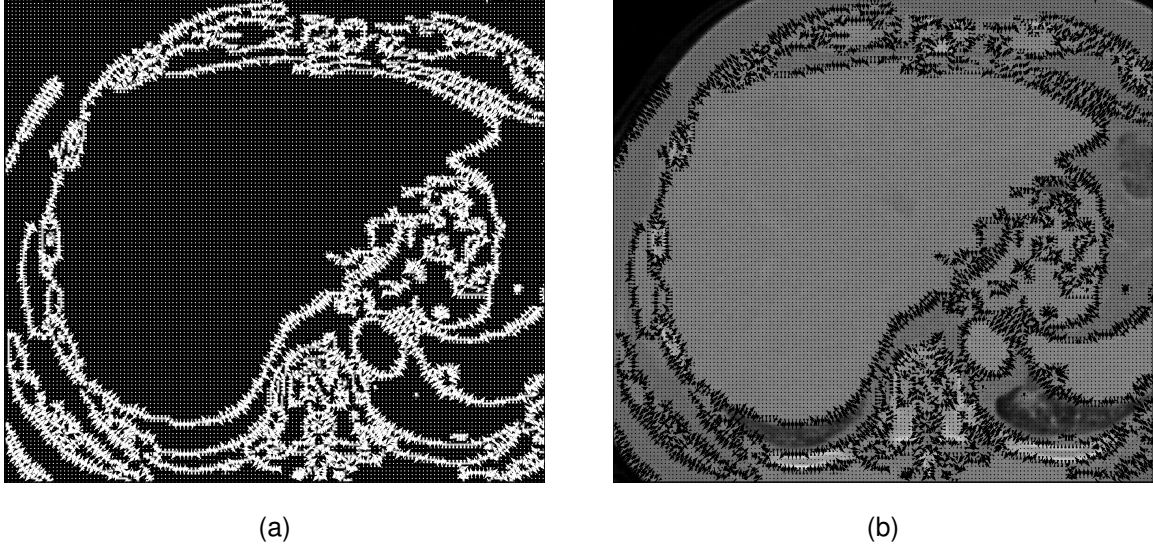


Figure 7: GVF field (a) on the edge map and (b) on the original CT image

user clicks, the second calculates all points at the determined position with the equation of a circle. An initial contour from each method is shown in Figure 8. After its placement, the initial contour  $\mathbf{x}(s)$  is iteratively deformed according to the following equation

$$\mathbf{x}(s, t) = \alpha \mathbf{x}_{ss}(s, t) - \beta \mathbf{x}_{ssss}(s, t) + \kappa \mathbf{v}(s) + \delta g(\mathbf{v}, s) \vec{n}(s), \quad (25)$$

where  $\kappa$  is a weighting factor for the GVF field  $\mathbf{v}(s)$  at contour position  $s$  and  $\delta$  is a weighting factor for an added balloon force  $\vec{n}(s)$ , which is computed as the outward unit normal vectors for the contour. The scalar function  $g(\mathbf{v}, s)$  is calculated according to  $g(\mathbf{v}, s) = \frac{1}{1+1000|\mathbf{v}(s)|}$  and serves as a weight to reduce  $\vec{n}(s)$  in regions close to object boundaries.

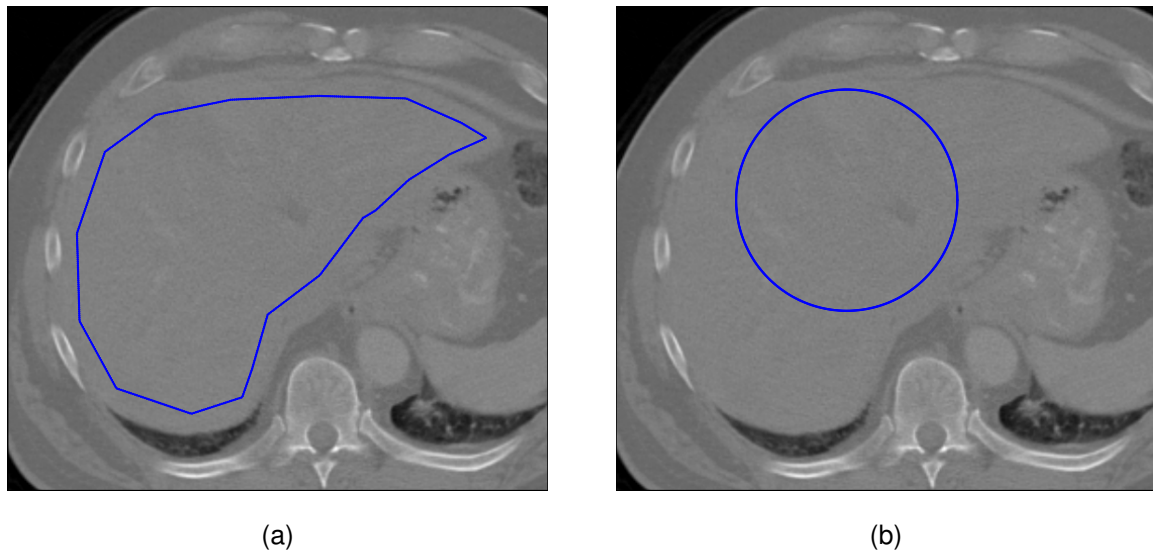


Figure 8: Initial contour (a) from multiple user clicks and (b) from placing a circle on the original CT image

The maximum number of iterations for the contour deformation was set to 300. However every 10th iteration, convergence in contour movement is tested by comparing the maximum difference between the contour from the current and the last iteration to a threshold. If the result is smaller or when the maximum number of iterations is reached, a binary mask is computed by checking which voxels are located inside the final contour, which can be seen in Figure 9.

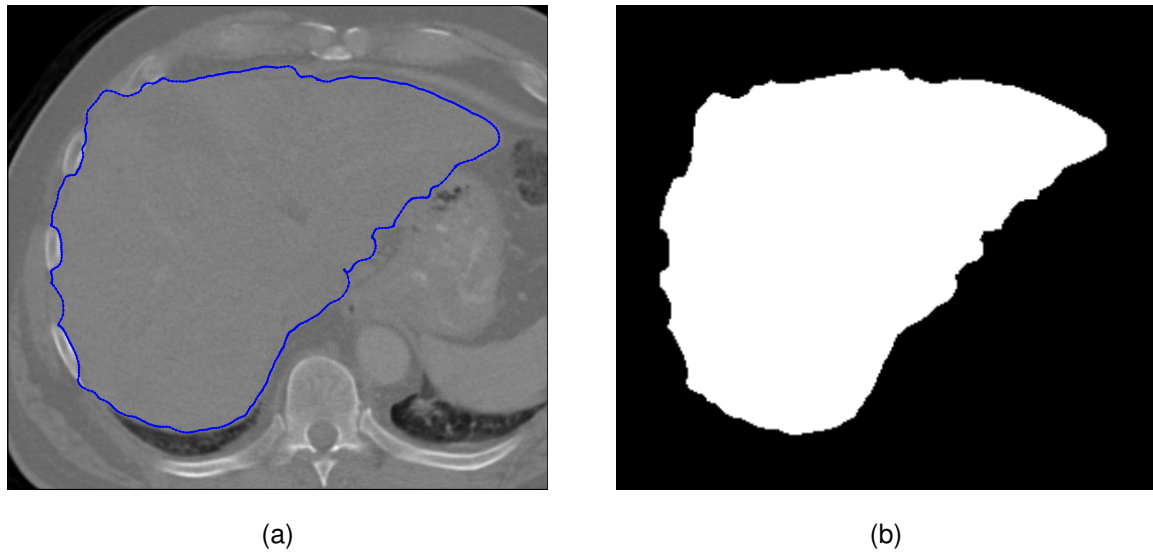


Figure 9: (a) Final contour on the original CT image (b) binary mask of the segmented liver

Afterwards for every  $x$  and  $y$  coordinate of the final contour the distance to the median of all respective coordinates is calculated. The next initial contour is obtained by subtracting half of the results from the final contour, which makes it smaller. The last step is to remove accumulations of multiple points in boundary regions for a more flexible contour deformation in the next slice.

### 2.1.2 Morphological GAC algorithm

The first step of the morphological GAC algorithm is to calculate a signed distance function for a circle, which the user places inside the liver by two clicks. The region where the signed distance function is greater than 0 is defined as the foreground of a binary LSF, which contains the initial contour at the 0.5 level set and is shown in Figure 10.

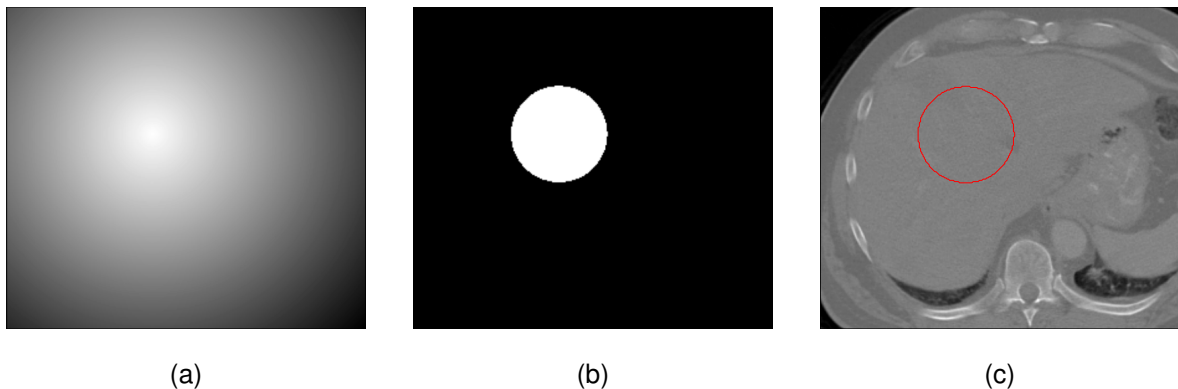


Figure 10: (a) Signed distance function, (b) initial binary LSF and (c) the 0.5 level set on the CT image

Image noise is reduced by anisotropic diffusion filtering as can be seen in Figure 5. Again the filter iterations were determined from the size of the bounding box. The smoothed CT image is then used to compute the stopping function  $g(I)$  from equation (20), where the parameter  $p$  is set to 2 in order to enhance the weak boundaries of the liver to adjacent organs. Figure 11 shows two possible stopping functions: the first from equation (19) and the second from equation (20), which is the one used for the morphological GAC algorithm.

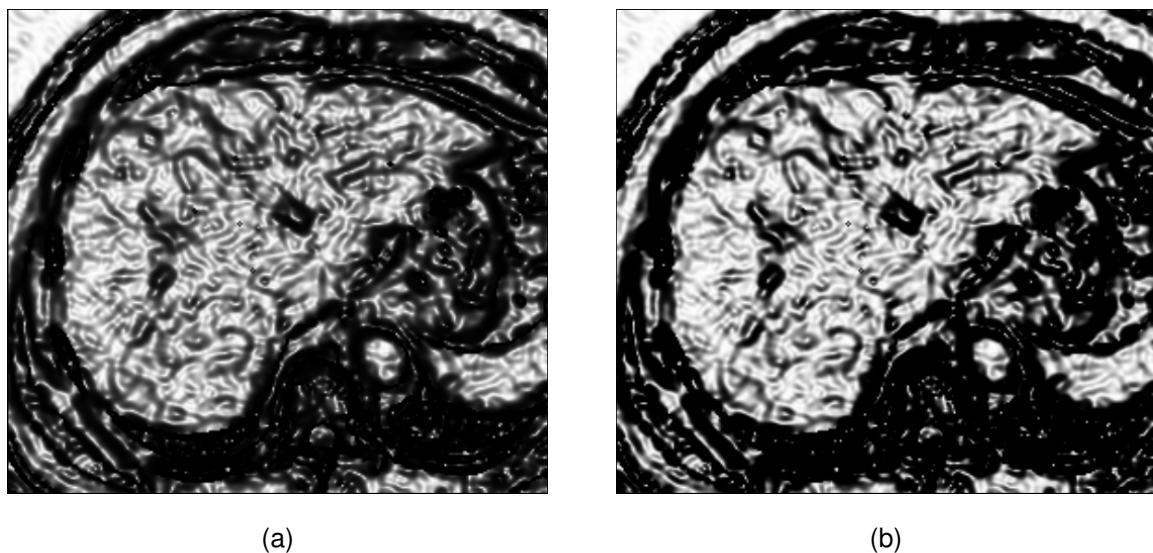


Figure 11:  $g(I)$  (a) from equation (19) and (b) from equation (20) with  $p = 2$

The morphological GAC model from Márquez et al. [2] replaces the balloon term from equation (18) with the binary erosion, the curvature term with the  $SI_d \circ IS_d$  operator and uses a discrete image attraction term. Based on Márquez et al. these terms are consecutively applied in every iteration  $n$  and the evolution of the binary LSF from  $u^n(x)$  to  $u^{n+1}(x)$  for every image point  $x$  was modelled as

$$\begin{aligned} u^{n+\frac{1}{3}}(x) &= \begin{cases} (D_d u^n)(x), & \text{if } g(I)(x) > \theta, \\ u^n(x), & \text{otherwise,} \end{cases} \\ u^{n+\frac{2}{3}}(x) &= \begin{cases} 1, & \text{if } \nabla u^{n+\frac{1}{3}} \nabla g(I) > 0, \\ 0, & \text{if } \nabla u^{n+\frac{1}{3}} \nabla g(I) < 0, \\ u^{n+\frac{1}{3}}, & \text{if } \nabla u^{n+\frac{1}{3}} \nabla g(I) = 0, \end{cases} \\ u^{n+1}(x) &= ((SI_d \circ IS_d)^\gamma u^{n+\frac{2}{3}})(x), \end{aligned} \quad (26)$$

where  $d$  is the size structuring element,  $\theta$  is a threshold for the discrete balloon force and  $\gamma$  is a parameter that controls the smoothing through the number of successive applications of  $SI_d \circ IS_d$ . The smallest reasonable value for  $d$  results in a 3x3 structuring element with a solid square for the binary dilation and the structuring elements from Figure 4 for  $SI_d \circ IS_d$ . This formulation for the morphological GAC is equivalent to equation (18) for  $\nu > 0$ , which corresponds to an outward balloon force.

The parameter  $\gamma$  was set to 2 and  $\theta$  was set proportional to the brightness of the image and inversely proportional to the size of the bounding box. Noise levels in CT images are inversely related to the number of detected x-ray photons [32]. A larger bounding box is mainly caused by a smaller pixel spacing which leads to less detected x-ray photons and thus to a darker image with more noise. In darker images with more noise  $\theta$  is smaller and the balloon force is stronger, which prevents the contour evolution from stopping at lower values of  $g(I)$  due to the higher noise levels.

The morphological GAC algorithm calculates the level set evolution according to equation (26) in a maximum number of 200 iterations. In order to detect convergence in the deformation of the binary LSF, every 10th iteration the sum of the difference between the current and the last LSF is calculated. If the result is smaller than a threshold that linearly increases with the number of iterations, or when the maximum number of iterations is reached, the final LSF equals the binary mask for the segmented liver, as can be seen in Figure 12.

As shown in Figure 10, the initial LSF for the next slice is then defined from the signed distance function of a circle, whose centre corresponds to the centroid of the final LSF from the previous slice and whose radius is proportional to its size.

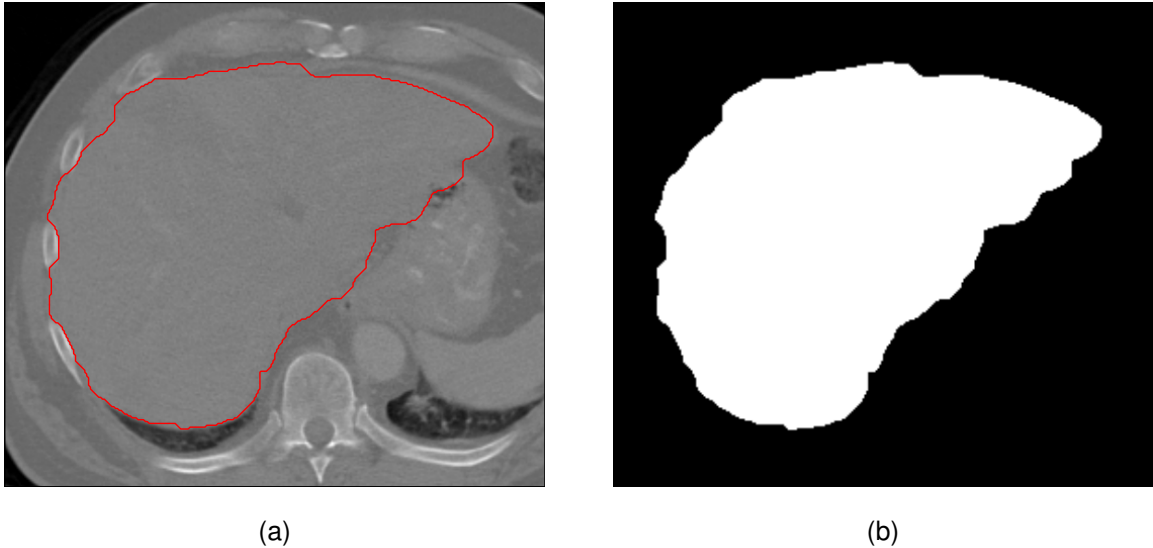


Figure 12: (a) Original CT image with the 0.5 level set of (b) the final binary LSF

Table 1: Slice thickness, pixel spacing and voxel size of all 21 CT datasets

Patient	Slice thickness [mm]	Pixel spacing [mm]	Voxel size [mm <sup>3</sup> ]
1 - 11	5	0.9765620 x 0.9765620	4.7683667
12 - 21	3	1.3671875 x 1.3671875	5.6076050

## 2.2 Evaluation

Both algorithms were tested on low-contrast CT datasets from 21 patients, which were provided in the standard Digital Imaging and Communications in Medicine (DICOM) file format [33]. The DICOM file format not only stores the image information, but also additional information about the patient, surface definitions and image registration. Each CT slice was stored in a separate DICOM file and a module for reading multiple DICOM files at once into Python was written in a previous project [34]. The program *ImageJ* [35] was used as an image viewer and for extracting information.

The datasets from patients 1 to 11 were supplied by the European Neuroendocrine Tumour Society (ENETS) Center of Excellence at the Zentralklinik Bad Berka. The datasets from patients 12 to 21 were provided by the Department of Radiation Oncology in the Division of Medical Radiation Physics from the Christian Doppler Laboratory for Medical Radiation Research for Radiation Oncology at the Medical University of Vienna. The slice thickness, the pixel spacing and the voxel size of these datasets are shown in Table 1. Despite different voxel geometries the resolution of all CT images is 512x512, which results in different field of views (FOVs), as shown in Figure 13 for the uncut start slices of patient 9 and 12.

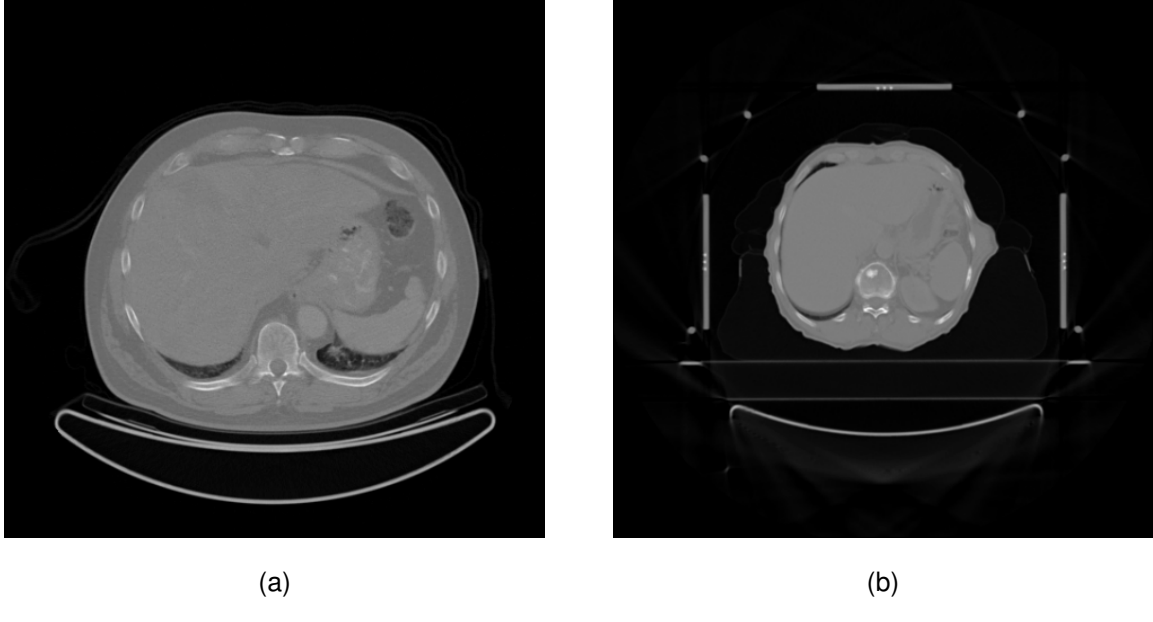


Figure 13: Uncut CT image (a) from patient 9 and (b) from patient 12

There are several measures for the performance of segmentation algorithms. The classical ones being based on region overlap, such as the Jaccard coefficient (JC), which is defined as

$$JC := \frac{|X \cap Y|}{|X \cup Y|}, \quad (27)$$

or the Dice Similarity coefficient (DS), that is calculated according to

$$DS := \frac{2|X \cap Y|}{|X| + |Y|}, \quad (28)$$

where  $X$  and  $Y$  are voxels of the same class from one and the other volume. If  $X$  and  $Y$  are the same region  $JC$  and  $DS$  are equal to one and they equal zero if  $X$  and  $Y$  have no overlap [36]. A common use of  $JC$  is in the volume overlap error (VOE), which is defined as  $100\%(1 - JC)$ . The relative volume difference (RVD) is given by  $100\%(|X| - |Y|)/|Y|$  [36].

The manual segmentation performed by Huber [1] was considered the ground truth for the evaluation. The RVD, the VOE and the DS were computed in a Python script with the the respective binary masks of the segmentation algorithms and the ones from manual segmentation. The liver volumes were calculated by multiplying the number of voxels classified as liver with the voxel size. The relative volume difference was computed with  $Y$  being the set of liver voxels from the manual segmentation.

## 3 Results

The evaluation results of the GVF snake algorithm are shown in Table 3. Depending on the size of the bounding box and the length and size of the initial contour the runtime was between 2 and 7 minutes per liver segmentation on a Intel® Core™ i7-4510U CPU @ 2 GHz and 16 GB RAM. The anisotropic diffusion filter, the modification of the edge map, the calculation of the GVF field and the determination of the voxels located inside the final contour were computationally the most demanding steps which can be sped up by multigrid methods and parallel implementations on the GPU [37].

Table 4 shows the evaluation results of the morphological GAC algorithm. The sizes of the bounding box and the foreground of the initial binary LSF influence the runtime, which was between 30 and 70 seconds per liver segmentation on the same setup that was used for the GVF snake algorithm. Sparse field or narrow-band techniques can be used to calculate the evolution of the binary LSF more efficiently. Both existing algorithms can also be optimized with the use of the Numba optimizing compiler or Cython extension modules [38].

In order to compare both algorithms the arithmetic mean and the standard deviation of the evaluation results were calculated, which can be seen in Table 2.

Table 2: Evaluation results of both algorithms as mean and standard deviation

Algorithm	RVD [%]	VOE [%]	DS
GVF snake	$-11.4 \pm 9.3$	$25.7 \pm 7.2$	$0.85 \pm 0.05$
Morph. GAC	$-3.9 \pm 6.1$	$17.3 \pm 2.8$	$0.91 \pm 0.02$

Table 3: Evaluation results of the GVF snake algorithm

Patient	RVD [%]	VOE [%]	DS	Patient	RVD [%]	VOE [%]	DS
1	-11.7	21.2	0.88	12	6.6	21.3	0.88
2	-2.8	15.4	0.92	13	-13.1	24.3	0.86
3	-8.2	18.5	0.90	14	-15.1	20.9	0.88
4	-13.8	27.0	0.84	15	-33.2	42.0	0.73
5	-8.3	22.6	0.87	16	-17.8	24.1	0.86
6	-12.1	33.9	0.80	17	-18.7	25.4	0.85
7	-16.1	22.2	0.87	18	-26.2	34.5	0.79
8	5.2	24.6	0.86	19	-16.0	25.6	0.85
9	-9.7	44.2	0.72	20	-4.2	22.7	0.87
10	-10.0	29.1	0.83	21	-16.1	23.1	0.87
11	2.1	17.3	0.91				

Table 4: Evaluation results of the morphological GAC algorithm

Patient	RVD [%]	VOE [%]	DS	Patient	RVD [%]	VOE [%]	DS
1	-1.4	14.7	0.92	12	11.9	19.0	0.90
2	-2.4	13.5	0.93	13	-5.0	16.0	0.91
3	-4.1	19.8	0.89	14	-10.9	19.1	0.89
4	-6.9	16.2	0.91	15	1.1	17.9	0.90
5	-1.6	16.0	0.91	16	-1.9	12.1	0.94
6	3.6	16.6	0.91	17	-2.6	15.9	0.91
7	-10.6	17.4	0.90	18	-14.3	24.6	0.86
8	-2.2	14.6	0.92	19	2.3	18.4	0.90
9	-11.4	22.1	0.88	20	-1.0	16.1	0.91
10	-9.1	19.1	0.89	21	-13.0	18.9	0.90
11	-2.1	15.1	0.92				

## 4 Discussion

As shown in Table 2, all evaluation results of the morphological GAC algorithm supersede GVF snake algorithm, which is partially caused by non-ideal edge maps of the liver. An ideal edge map shows the whole liver boundary as edge while at the same time edges inside the liver are suppressed. The modification by removing small edges usually improved the edge map, however in some CT images large gaps in the liver edge were created or large edges inside the liver could not be removed, which can be seen in Figure 14. Such edges lead to incorrect segmentations of the liver.

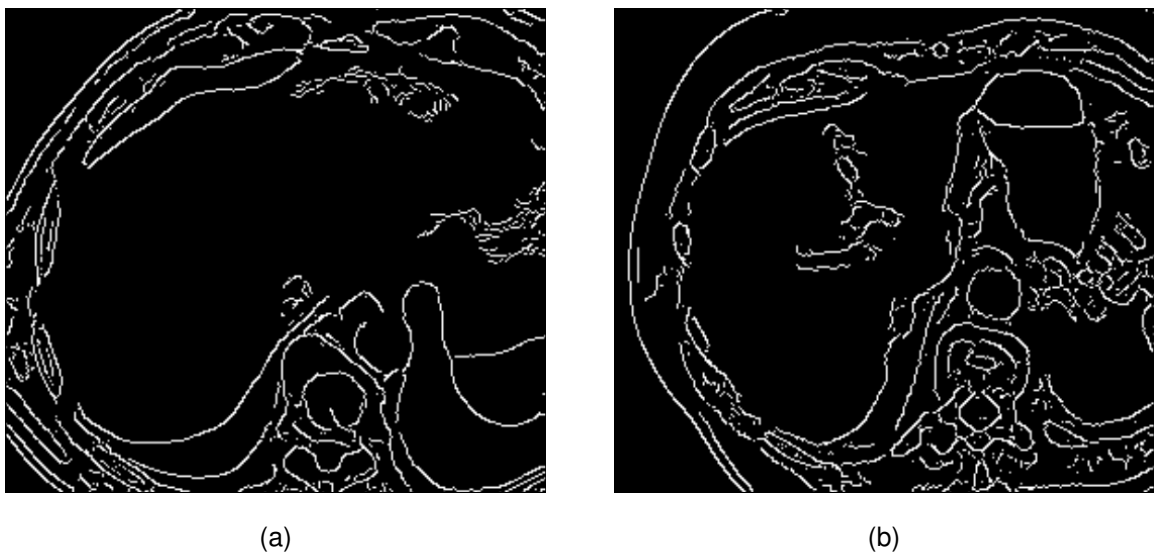


Figure 14: Modified edge map with (a) large gaps in the liver edge and (b) large edges inside the liver

Figures 15 and 16 show liver segmentations of both algorithms in CT images with a concise concavity in the liver boundary and particular low contrast between the liver and adjacent organs due to large pixel spacing. As can be seen the GVF snake algorithm cannot adapt to the concavity since the shape of the initial contour is fundamentally different. Thus for the positioning of the initial contour on the start slice the method with multiple user clicks is preferred. The progression of the contour into concavities is inhibited by an insufficient number of contour points in these regions and subsequent restrictions due to internal forces. Simply increasing the number of points without increasing the weighting of the internal forces leads to stability issues, i.e. loops in the final contour. The main advantage of the GVF snake algorithm is that internal forces prevent the contour from leaking into small gaps of the liver's edge.

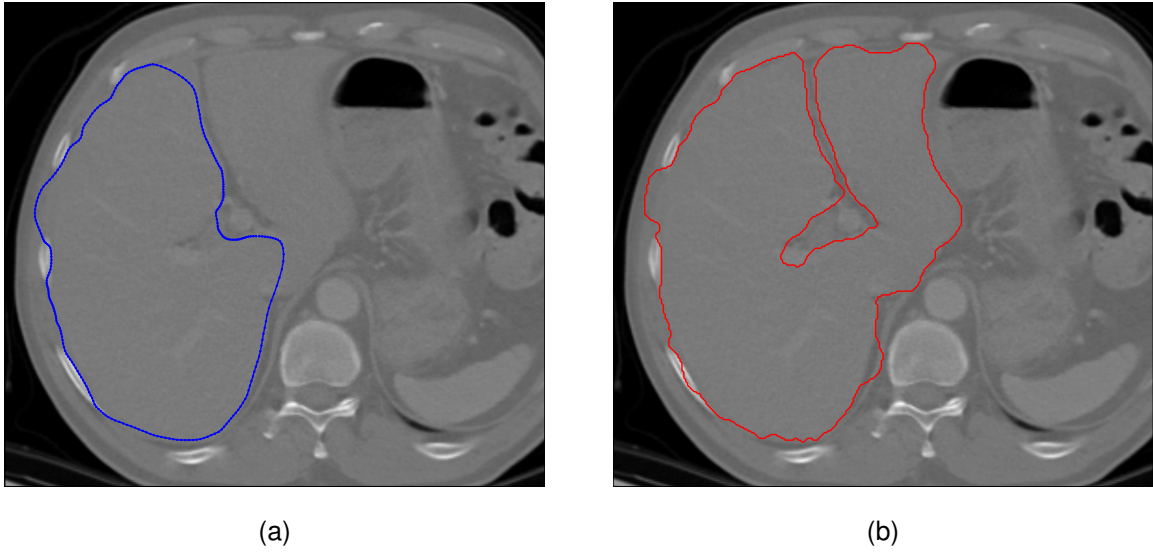


Figure 15: Liver segmentation of (a) GVF snake and (b) morphological GAC algorithms in a CT image with a concave concavity in the liver boundary

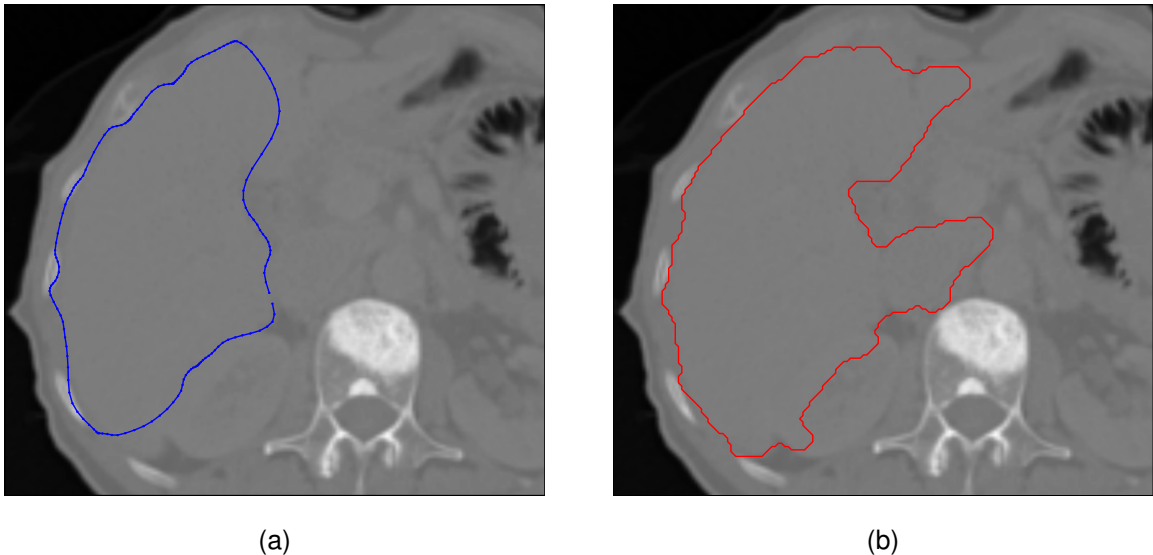


Figure 16: Liver segmentation of (a) GVF snake and (b) morphological GAC algorithms in a CT image with particular low contrast between the liver and adjacent organs due to large pixel spacing

As the contour deformation is independent from initialization the segmentation results of the morphological GAC algorithm are not influenced by the shape of the liver boundary with the exception that the contour cannot progress into hysteric liver boundaries as the curvature term removes singularities by smoothing the contour. The main reason for segmentation errors of the morphological GAC algorithm can be found in the determination of the parameter  $\theta$ , which is not optimal for every CT image. An excessive balloon force resulting from a too small  $\theta$  can cause the contour to pass through faint liver boundaries, which originate from low contrast to adjacent organs due to large pixel spacing.

The evaluation results from this thesis do not outline the full capabilities of deformable models since both algorithms can be improved. For instance Liu et al. [39] modified the edge map for a GVF snake by suppressing edges inside a liver template, that is obtained with thresholding, before applying a concavity removal algorithm. An alternative to GVF as an external force for active contours is vector field convolution [40] which offers superior noise robustness and is computationally less demanding. After anisotropic diffusion filtering Suzuki et al. [41] used a Gaussian filter for the calculation of the stopping function  $g(I)$ . The balloon term of the GAC model was altered by Siddiqi et al. [42] to provide a stronger attraction force to boundaries. In general the performance of semi-automatic liver segmentation algorithms can be improved by increasing the amount of interaction with an expert [43].

Withey and Koles [44] divided methods for medical image segmentation into three generations in accordance with ascending algorithmic complexity. Deformable models were numbered among the second generation because they do not incorporate prior-knowledge to improve the accuracy and robustness of the segmentation. According to Sharp et al. [45] deformable models are often combined with statistical shape models or atlas-based segmentation to include shape and appearance characteristics of the desired anatomical structure and therewith to overcome the boundary difficulties in CT images with insufficient soft tissue contrast. Furthermore Sharp et al. concluded that at the time of April 2014 for the North American market all commercial automated segmentation systems used atlas-based segmentation, some of which in combination with statistical shape models [45].

## 4.1 Conclusion

After evaluating all segmentation results, the morphological GAC algorithm outperformed the GVF snake algorithm regarding RVD, VOE, DS and also runtime. However considerable issues with the evaluation are that the ground truth is unknown and that the used CT datasets are not publicly accessible. An objective comparison on a common database for low-contrast CT images would increase the transparency of the evaluation. Further improvements to the morphological GAC algorithm are needed as the application in clinical practice generally requires a higher accuracy and robustness of the segmentation results.

# Bibliography

- [1] A. Huber. Comparison of manual, 2D semi-automatic and 3D fully-automatic kidney and liver segmentation based on the evaluation of gradient vector flow fields on CT images. *Bachelor's Paper, Degree Program Biomedical Engineering at University of Applied Sciences Technikum Wien*, Apr 2015.
- [2] P. Márquez-Neila, L. Baumela, and L. Alvarez. A morphological approach to curvature-based evolution of curves and surfaces. *IEEE Transactions on Pattern Analysis and Machine Intelligence*, 36(1):2–17, Jan 2014.
- [3] Neeraj Sharma and Lalit M. Aggarwal. Automated medical image segmentation techniques. *J Med Phys.*, 35(1):3–14, Jan-Mar 2010.
- [4] Y. Masutani, K. Uozumi, Masaaki Akahane, and Kuni Ohtomo. Liver CT image processing: A short introduction of the technical elements. *European Journal of Radiology*, 58(2):246 – 251, May 2006.
- [5] S. R. Abdel-Misih and M. Bloomston. Liver anatomy. *Surg. Clin. North Am.*, 90(4):643–653, Aug 2010.
- [6] D. L. Pham, C. Xu, and J. L. Prince. Current methods in medical image segmentation. *Annu Rev Biomed Eng*, 2:315–337, 2000.
- [7] Gavril Tsechpenakis. Deformable model-based medical image segmentation. In *Multi Modality State-of-the-Art Medical Image Segmentation and Registration Methodologies: Volume 1*, pages 33–67. Springer, May 2011.
- [8] Chenyang Xu, A. Yezzi, and J. L. Prince. On the relationship between parametric and geometric active contours. In *Signals, Systems and Computers, 2000. Conference Record of the Thirty-Fourth Asilomar Conference on*, volume 1, pages 483–489 vol.1, Oct 2000.
- [9] Chenyang Xu, Dzung L. Pham, and Jerry L. Prince. Image segmentation using deformable models. In J. Michael Fitzpatrick and Milan Sonka, editors, *Handbook of Medical Imaging. Vol.2 Medical Image Processing and Analysis*, pages 175–272. SPIE Publications, Apr 2009.
- [10] Michael Kass, Andrew Witkin, and Demetri Terzopoulos. Snakes: Active contour models. *International Journal of Computer Vision*, 1(4):321–331, Jan 1988.

- [11] Chenyang Xu and Jerry L. Prince. Snakes, shapes, and gradient vector flow. *IEEE TRANSACTIONS ON IMAGE PROCESSING*, 7(3):359–369, Mar 1998.
- [12] Chenyang Xu and J. L. Prince. Gradient vector flow: a new external force for snakes. In *Computer Vision and Pattern Recognition, 1997. Proceedings., 1997 IEEE Computer Society Conference on*, pages 66–71, Jun 1997.
- [13] Z. Zheng and R. Zhang. A Fast GVF Snake Algorithm on the GPU. *Research Journal of Applied Sciences, Engineering and Technology*, 4(24):5565–5571, Dec 2012.
- [14] X. Han, C. Xu, and J. L. Prince. Fast numerical scheme for gradient vector flow computation using a multigrid method. *IET Image Processing*, 1(1):48–55, March 2007.
- [15] Ross T. Whitaker. A level-set approach to 3d reconstruction from range data. *International Journal of Computer Vision*, 29(3):203–231, Sep 1998.
- [16] J. A. Sethian. A fast marching level set method for monotonically advancing fronts. *Proc. Natl. Acad. Sci. U.S.A.*, 93(4):1591–1595, Feb 1996.
- [17] Vicent Caselles, Ron Kimmel, and Guillermo Sapiro. Geodesic active contours. *International Journal of Computer Vision*, 22(1):61–79, Feb 1997.
- [18] Vicent Caselles, Francine Catté, Tomeu Coll, and Françoise Dibos. A geometric model for active contours in image processing. *Numerische Mathematik*, 66(1):1–31, Dec 1993.
- [19] D. Adalsteinsson and J.A Sethian. The fast construction of extension velocities in level set methods. *Journal of Computational Physics*, 148(1):2 – 22, Jan 1999.
- [20] J. Weickert, B. H. Romeny, and M. A. Viergever. Efficient and reliable schemes for nonlinear diffusion filtering. *IEEE Trans Image Process*, 7(3):398–410, Mar 1998.
- [21] R. Goldenberg, R. Kimmel, E. Rivlin, and M. Rudzsky. Fast geodesic active contours. *IEEE Transactions on Image Processing*, 10(10):1467–1475, Oct 2001.
- [22] G. Papandreou and P. Maragos. Multigrid geometric active contour models. *IEEE Trans Image Process*, 16(1):229–240, Jan 2007.
- [23] Edward R. Dougherty and Roberto A. Lotufo. *Hands-on Morphological Image Processing (SPIE Tutorial Texts in Optical Engineering Vol. TT59)*. SPIE Publications, Jul 2003.
- [24] Luis Alvarez, Frédéric Guichard, Pierre Louis Lions, and Jean Michel Morel. Axioms and fundamental equations of image processing. *Archive for Rational Mechanics and Analysis*, 123(3):199–257, Sep 1993.
- [25] Stéfan van der Walt, S. Chris Colbert, and Gaël Varoquaux. The numpy array: A structure for efficient numerical computation. *Computing in Science & Engineering*, 13(2):22–30, Mar 2011.

- [26] Eric Jones, Travis Oliphant, Pearu Peterson, et al. SciPy: Open source scientific tools for Python, 2001-, <http://www.scipy.org/>. [Online; accessed 2016-04-20].
- [27] G. Bradski. *Dr. Dobb's Journal of Software Tools*, Nov 2000.
- [28] John D. Hunter. Matplotlib: A 2D graphics environment. *Computing in Science & Engineering*, 9(3):90–95, May-June 2007.
- [29] P. Perona and J. Malik. Scale-space and edge detection using anisotropic diffusion. *IEEE Transactions on Pattern Analysis and Machine Intelligence*, 12(7):629–639, Jul 1990.
- [30] P. Sprawls. AAPM tutorial. CT image detail and noise. *RadioGraphics*, 12(5):1041–1046, Sep 1992.
- [31] J. Canny. A computational approach to edge detection. *IEEE Transactions on Pattern Analysis and Machine Intelligence*, PAMI-8(6):679–698, Nov 1986.
- [32] L. W. Goldman. Principles of CT: radiation dose and image quality. *J Nucl Med Technol*, 35(4):213–225, Dec 2007.
- [33] NEMA PS3 / ISO 12052. Digital Imaging and Communications in Medicine (DICOM) Standard. *National Electrical Manufacturers Association, Rosslyn, VA, USA*, 1993-, <http://medical.nema.org/>. [Online; accessed 2016-04-20].
- [34] M. Blaickner, M. Dulovits, G. Dietmar, Chr. Doppler, H. Kulkarni, S. Wiessalla, C. Schuchardt, and R. Baum. Novel computational tools for dosimetry, segmentation and treatment planning in targeted radionuclide therapy. *J Nucl Med.*, 55(Supplement 1):2076, Jun 2014.
- [35] W.S. Rasband. ImageJ. *U.S. National Institutes of Health, Bethesda, Maryland, USA*, 1997-, <http://imagej.nih.gov/ij/>. [Online; accessed 2016-04-20].
- [36] Rubén Cárdenes, Meritxell Bach, Ying Chi, Ioannis Marras, Rodrigo Luis, Mats Anderson, Peter Cashman, and Matthieu Bultelle. *Computer Analysis of Images and Patterns: 12th International Conference, CAIP 2007, Vienna, Austria, August 27-29, 2007. Proceedings*, chapter Multimodal Evaluation for Medical Image Segmentation, pages 229–236. Springer Berlin Heidelberg, Berlin, Heidelberg, Aug 2007.
- [37] E. Smistad, T. L. Falch, M. Bozorgi, A. C. Elster, and F. Lindseth. Medical image segmentation on GPUs—a comprehensive review. *Med Image Anal*, 20(1):1–18, Feb 2015.
- [38] Stefan Behnel, Robert Bradshaw, Craig Citro, Lisandro Dalcin, Dag Sverre Seljebotn, and Kurt Smith. Cython: The best of both worlds. *Computing in Science & Engineering*, 13(2):31–39, Apr 2011.
- [39] F. Liu, B. Zhao, P. K. Kijewski, L. Wang, and L. H. Schwartz. Liver segmentation for CT images using GVF snake. *Med Phys*, 32(12):3699–3706, Dec 2005.

- [40] B. Li and S. T. Acton. Active contour external force using vector field convolution for image segmentation. *IEEE Trans Image Process*, 16(8):2096–2106, Aug 2007.
- [41] Kenji Suzuki, Ryan Kohlbrenner, Mark L. Epstein, Ademola M. Obajuluwa, Jianwu Xu, and Masatoshi Hori. Computer-aided measurement of liver volumes in CT by means of geodesic active contour segmentation coupled with level-set algorithms. *Medical Physics*, 37(5):2159–2166, Apr 2010.
- [42] K. Siddiqi, Y. B. Lauziere, A. Tannenbaum, and S. W. Zucker. Area and length minimizing flows for shape segmentation. *IEEE Transactions on Image Processing*, 7(3):433–443, Mar 1998.
- [43] T. Heimann, B. van Ginneken, M. A. Styner, Y. Arzhaeva, V. Aurich, C. Bauer, A. Beck, C. Becker, R. Beichel, G. Bekes, F. Bello, G. Binnig, H. Bischof, A. Bornik, P. M. Cashman, Y. Chi, A. Cordova, B. M. Dawant, M. Fidrich, J. D. Furst, D. Furukawa, L. Grenacher, J. Hornegger, D. Kainmuller, R. I. Kitney, H. Kobatake, H. Lamecker, T. Lange, J. Lee, B. Lennon, R. Li, S. Li, H. P. Meinzer, G. Nemeth, D. S. Raicu, A. M. Rau, E. M. van Rikxoort, M. Rousson, L. Rusko, K. A. Saddi, G. Schmidt, D. Seghers, A. Shimizu, P. Slagmolen, E. Sorantin, G. Soza, R. Susomboon, J. M. Waite, A. Wimmer, and I. Wolf. Comparison and evaluation of methods for liver segmentation from CT datasets. *IEEE Trans Med Imaging*, 28(8):1251–1265, Aug 2009.
- [44] D. J. Withey and Z. J. Koles. Medical image segmentation: Methods and software. In *Noninvasive Functional Source Imaging of the Brain and Heart and the International Conference on Functional Biomedical Imaging, 2007. NFSI-ICFBI 2007. Joint Meeting of the 6th International Symposium on*, pages 140–143, Oct 2007.
- [45] G. Sharp, K. D. Fritscher, V. Pekar, M. Peroni, N. Shusharina, H. Veeraraghavan, and J. Yang. Vision 20/20: perspectives on automated image segmentation for radiotherapy. *Med Phys*, 41(5):050902, May 2014.

# List of Figures

Figure 1	(a) Binary image with (b) structuring element placed at two locations, taken from [23]	6
Figure 2	(a) Dilation of a binary image by (b) a disk, taken from [23]	7
Figure 3	(a) Erosion of a binary image by (b) a rectangle combined with a semi-disk, taken from [23]	7
Figure 4	Four 3x3 structures for the discrete curvature morphological operator (dark blue = active), taken from [2]	8
Figure 5	CT image (a) before and (b) after anisotropic diffusion filtering	10
Figure 6	Edge map (a) before and (b) after the removal of small edges	11
Figure 7	GVF field (a) on the edge map and (b) on the original CT image	11
Figure 8	Initial contour (a) from multiple user clicks and (b) from placing a circle on the original CT image	12
Figure 9	(a) Final contour on the original CT image (b) binary mask of the segmented liver	12
Figure 10	(a) Signed distance function, (b) initial binary LSF and (c) the 0.5 level set on the CT image	13
Figure 11	$g(I)$ (a) from equation (19) and (b) from equation (20) with $p = 2$	13
Figure 12	(a) Original CT image with the 0.5 level set of (b) the final binary LSF	15
Figure 13	Uncut CT image (a) from patient 9 and (b) from patient 12	16
Figure 14	Modified edge map with (a) large gaps in the liver edge and (b) large edges inside the liver	19
Figure 15	Liver segmentation of (a) GVF snake and (b) morphological GAC algorithms in a CT image with a concise concavity in the liver boundary	20
Figure 16	Liver segmentation of (a) GVF snake and (b) morphological GAC algorithms in a CT image with particular low contrast between the liver and adjacent organs due to large pixel spacing	20

## List of Tables

Table 1	Slice thickness, pixel spacing and voxel size of all 21 CT datasets . . . . .	15
Table 2	Evaluation results of both algorithms as mean and standard deviation . . . . .	17
Table 3	Evaluation results of the GVF snake algorithm . . . . .	18
Table 4	Evaluation results of the morphological GAC algorithm . . . . .	18

# List of Abbreviations

<b>CT</b>	Computed Tomography
<b>GVF</b>	Gradient Vector Flow
<b>GAC</b>	Geodesic Active Contour
<b>LSF</b>	Level Set Function
<b>AIT</b>	Austrian Institute of Technology
<b>DICOM</b>	Digital Imaging and Communications in Medicine
<b>ENETS</b>	European Neuroendocrine Tumour Society
<b>FOV</b>	Field Of View
<b>JC</b>	Jaccard Coefficient
<b>DS</b>	Dice Similarity coefficient
<b>VOE</b>	Volume Overlap Error
<b>RVD</b>	Relative Volume Difference